Microwave spectroscopy of the calcium $4snf \rightarrow 4s(n+1)d$, $4sng$, $4snh$, $4sni$, and $4snk$ transitions

J. Nunkaew[1,*] and T. F. Gallagher[2]

[1]*Department of Physics and Materials Science, Faculty of Science, Chiang Mai University, Chiang Mai 50200, Thailand*

[2]*Department of Physics, University of Virginia, Charlottesville, Virginia 22904, USA*

(Received 27 January 2015; published 10 April 2015)

We observe the microwave transitions of calcium from the $4snf$ states to the $4s(n+1)d$, $4sng$, $4snh$, $4sni$, and $4snk$ states for $18 \leqslant n \leqslant 23$ using delayed field ionization as the state selective detection technique. The observed intervals between the $\ell \geqslant 5$ states can be analyzed to extract the Ca^+ ionic dipole (α_d) and quadrupole (α_q) polarizabilities using two nonadiabatic core polarization models. Using these two models we determine the ionic dipole and quadrupole polarizabilities to be $75.3a_0^3 < \alpha_d < 76.9a_0^3$ and $206a_0^5 < \alpha_q < 1590a_0^5$, respectively.

DOI: 10.1103/PhysRevA.91.042503 PACS number(s): 32.30.−r, 32.10.Dk, 32.80.Rm

I. INTRODUCTION

In recent years, much effort has been invested in developing a precise optical frequency standard, and a proposed candidate is the quadrupole $4s_{1/2} - 3d_{5/2}$ transition of the Ca^+ ion [1,2]. An additional attraction of Ca^+ is that it can be cooled by Doppler cooling to very low temperatures by using this transition in conjunction with the dipole allowed $3d_{5/2} - 3p_{3/2}$ transition [1]. The absolute frequency of the Ca^+ $4s_{1/2} - 3d_{5/2}$ transition has been measured with an uncertainty of 1 Hz, a fractional accuracy of one part in 10^{15}, which is within a factor of 3 of the fractional uncertainty of the present Cs clock [3]. While an optical transition provides a transition with a higher quality factor, the transition also has a much larger blackbody radiation (BBR) shift, and the BBR shift is one of the largest shifts in an optical clock. In the Ca^+ clock transition the BBR shift is calculated to be 0.4 Hz at room temperature, $T = 300$ K [1,2,4]. Since the BBR shift is unavoidable and scales as T^4 [5], it is essential to understand it well.

The BBR shift is proportional to the difference in the dipole polarizabilities α_d of the two ionic states of the clock transition. While it is possible to calculate the polarizabilities, due to the charge of the ion the polarizabilities are difficult to measure directly, and other approaches must be used to check the validity of the calculations. While measurements of oscillator strengths and lifetimes are often used, an alternative approach is one initially suggested by Mayer and Mayer, measuring the energy intervals between higher ℓ Rydberg states of the neutral atom [6]. Here ℓ is the orbital angular momentum of the Rydberg electron. The field and gradient from the Rydberg electron polarize the ionic core, depressing the energy levels below the hydrogenic energy of $-1/2n^2$, where n is the principal quantum number of the Rydberg electron. We use atomic units unless specified otherwise. Since an electron in a lower ℓ state comes closer to the ionic core, the polarization shift increases with decreasing ℓ. This approach is only valid if the Rydberg electron does not penetrate the ionic core, which is why it is limited to high ℓ states. The inner turning point of a Rydberg $n\ell$ atom is given by $r_\ell \cong \ell(\ell+1)/2$, and $r_\ell = 15a_0$ for $\ell = 5$. Since the Ca^+ $4s_{1/2}$ wave function is similar in size to the H $1s$ wave function, less than 0.02% of the ground-state probability distribution is found at radial distances beyond $r = 15a_0$, so it seems that Ca $4sn\ell$ states of $\ell \geqslant 5$ should be nonpenetrating states. Here r is the distance of the Rydberg electron from the ionic core.

Here we report measurements of the Ca $4snf - 4sng - 4snh - 4sni - 4snk$ intervals, made using a delayed field ionization approach. Our data show that the adiabatic model of Mayer and Mayer is inadequate, and we have fit our measurements to two core polarization models which take into account the nonadiabatic effects not considered in the approach of Mayer and Mayer. These analyses yield values for the dipole polarizability in reasonable agreement with the calculated value. However, the two values we extract for the quadrupole polarizability are much smaller and much larger than the calculated value. We have also measured the $4snf \rightarrow 4s(n+1)d$ intervals. These intervals, combined with high-resolution optical spectroscopy could allow a better determination of the Ca^+ polarizabilities. In the sections which follow we describe our approach, present our experimental results, and analyze them using several variants of core polarization analysis.

II. EXPERIMENTAL APPROACH

We excite neutral Ca atoms in a thermal beam from the ground state to a Rydberg state using three laser beams. The Ca beam intersects the laser beams at a 90° angle between two parallel horizontal copper plates separated by 1.2-cm-long ceramic standoffs. The laser beams are focused to 1 mm diameters where they intersect the Ca beam. Ground-state $4s^2$ atoms are excited to the $4s4p$, $4s4d$, and $4snf$ states by 422.791 nm, 732.816 nm, and ∼850 nm laser pulses, respectively, as shown in Fig. 1. The last laser is tunable over the range from 847 to 857 nm to excite the $4snf$ states of $18 \leqslant n \leqslant 23$. A 1-$\mu$s-long microwave pulse starts 50 ns after the last laser pulse to excite the $4snf$ state to the $4sng$ and $4snh$ states by the one-photon and two-photon transitions, respectively. The $4snf \rightarrow 4sni$ and $4snf \rightarrow 4snk$ transitions are the three-photon and four-photon transitions. To drive the three-photon and four-photon excitations, in addition to a 1 μs microwave pulse, we use a continuous wave (cw) radio frequency (rf) field of frequency between 3.5 and 5 GHz. The rf and microwave fields are generated by a Hewlett-Packard (HP) 8257D analog signal generator and 83620A synthesized sweep generator, respectively. The microwave sweep generator produces a cw output from 10 MHz to 20 GHz, which is

*jn8h@virginia.edu

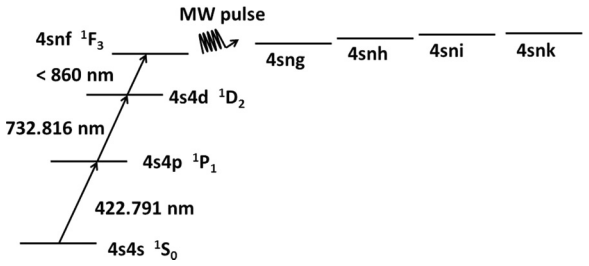

FIG. 1. Laser excitation scheme of the experiment.

formed into pulses by a General Microwave DM862D switch. The required microwave frequencies to drive the transitions range from 23 to 75 GHz. Therefore, several frequency multipliers, a Narda DBS 2640X220 active doubler, a Narda DBS 4060X410 active quadrupler, and a Pacific Millimeter V2W0 passive doubler, are used to multiply the synthesizer frequency to the desired frequency. The power output of the frequency multipliers ranges from 5 mW to 100 mW. The microwaves propagate through WR28 waveguide and a waveguide feedthrough to a WR28 horn inside the vacuum chamber. The cw rf propagates through a coaxial cable and a SMA feedthrough to the coaxial-to-waveguide adapter and is launched by a WR187 horn inside the chamber.

To discriminate between the $4snℓ$ states of $ℓ > 3$ and the $4snf$ state, we take advantage of the $ℓ$ dependence of the lifetimes of Ca Rydberg atoms. The higher angular momentum Rydberg states live longer than the lower ones [7,8], and we use the technique of delayed field ionization (DFI). The lifetime of the $4s25f$ state has been measured to be ∼2.5(5) μs [8], and using the n^3 scaling law we find that the lifetimes of the $4snf$ states of $18 \leqslant n \leqslant 23$ fall in the range from 0.9 to 1.9 μs. Therefore, if we wait long enough after the microwave pulse, more than 5 μs, atoms in the $4snf$ states decay significantly compared to atoms in the $4snℓ$ states of $ℓ > 3$. Typically, we apply a negative high voltage pulse to the bottom plate 8 to 10 μs after the microwave pulse to field ionize the surviving Rydberg atoms and drive the resulting electrons to the microchannel plate (MCP) detector. The timing of the experiment is shown in Fig. 2. Using this approach a large increase in the number of detected atoms is observed when the microwave field drives the transition from the $4snf$ state at resonance. To detect transitions from the $4snf$ states to the $4s(n+1)d$ states we take advantage of the fact that the lifetimes of the $4s(n+1)d$ states are an order of magnitude shorter than those of the $4snf$ states. A delay of only 2 μs

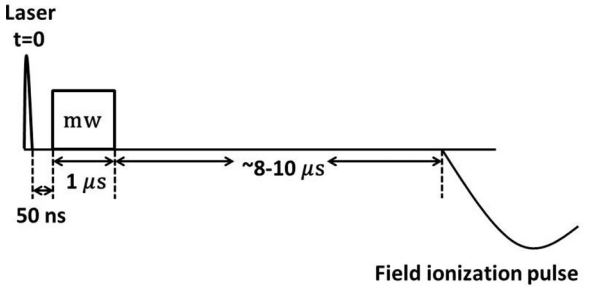

FIG. 2. Timing sequence of the experiment.

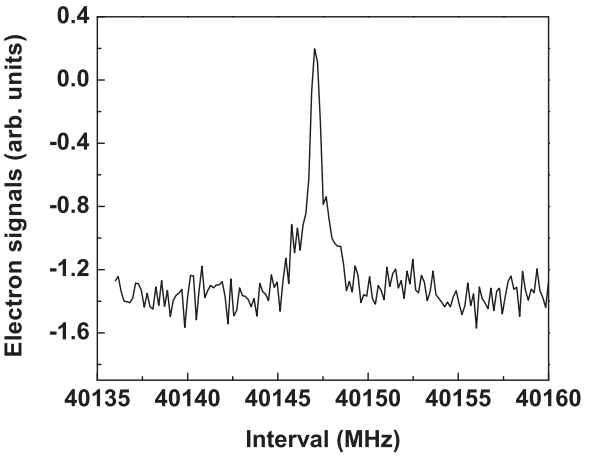

FIG. 3. One-photon $4s22f \rightarrow 4s22g$ resonance. The linewidth of the resonance is ∼1 MHz which is a transform limited linewidth of a 1 μs microwave pulse.

is used, and a decrease in signal is observed at resonance. Frequency shifts due to the stray electric field are minimized by observing the microwave resonance with different bias voltages on the plates and fitting the resonant frequencies to a quadratic bias voltage dependence. We then set the bias voltage to the minimum frequency shift. In this experiment, the frequency shift due to the stray electric field is in all cases less than 1 MHz. The experiment is repeated every 50 ms, and the signals are averaged over many laser shots.

III. EXPERIMENTAL OBSERVATIONS

A. One-photon $4snf \rightarrow 4sng$ intervals

For the one-photon transition, $4snf \rightarrow 4sng$, the microwave power was attenuated until the power broadening was eliminated. We observed one resonant peak for each n. Since the optical excitation is to the $4snf$ $^1F_3$ state we assign the states we observe in the microwave transitions as $^1G_4$ states. A typical resonance is shown in Fig. 3, and the observed intervals are given in Table I. We did not attempt to eliminate the Earth's magnetic field. In the Earth's magnetic field one might expect linewidths of ∼2–3 MHz. However, the typical linewidth of a $^1F_3 - {}^1G_4$ resonance is ∼1 MHz, the transform limited linewidth of a 1 μs microwave pulse. The narrow linewidths occur because the one-photon transitions are between the two singlet states, which have the same Landé g_j factors. Hence all the $\Delta m_j = 0$ transitions occur at the same frequency, resulting in the narrow lines [9].

TABLE I. $nf - ng$ observed frequencies.

n	Observed frequency (MHz)
18	72891.40(1)
19	62222.19(1)
20	53150.84(2)
21	46053.01(25)
22	40147.03(1)
23	35462.65(5)

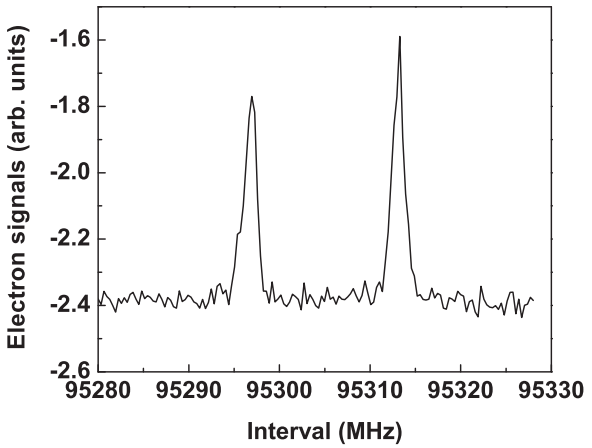

FIG. 4. Two-photon $4s18f \rightarrow 4s18h$ resonances. The two resonances are separated by the K splitting of the $4s18h$ state.

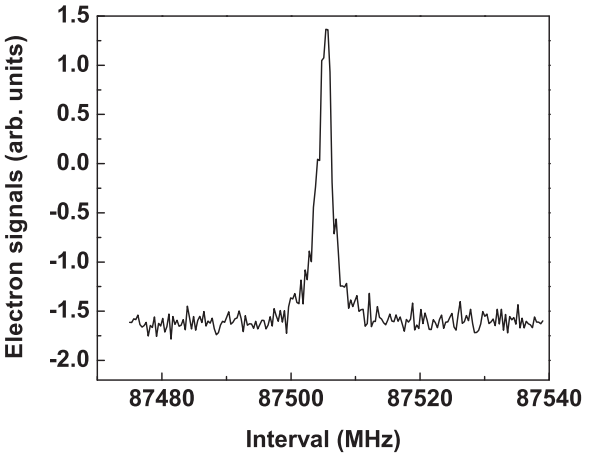

FIG. 5. Three-photon $4s19f \rightarrow 4s19i$ resonance at relative microwave power 0.63 and at relative rf power 1.0. The K splitting of the $4s19i$ states cannot be resolved due to the Earth's magnetic-field broadening.

B. Two-photon $4snf \rightarrow 4snh$ intervals

For the two-photon transition, $4snf \rightarrow 4snh$, we observed two resonant peaks for each n suggesting that the higher ℓ states, $\ell \geqslant 5$, are not singlets and triplets. The states are described by coupling the total angular momentum of the core $\vec{j}_c$ to the orbital angular momentum $\vec{\ell}$ of the Rydberg electron to form $\vec{K}$. Explicitly,

$$\vec{K} = \vec{j}_c + \vec{\ell}. \tag{1}$$

The splitting between the two K levels is due to the indirect spin orbit splitting [10,11]. We ignore the spin of the Rydberg electron. For the Ca $4sn\ell$ states, $j_c = 1/2$; therefore, $K = \ell \pm 1/2$. Hence, for each ℓ state we observe two transitions from the $4snf$ to the $4sn\ell$ states, corresponding to $K = \ell + 1/2$ and $K = \ell - 1/2$. To correct for the small ac Stark shift due to the microwave field, 1.8 MHz at the highest power we used, the resonances were observed at different microwave powers, and the resonance frequencies were extrapolated linearly to zero microwave power to obtain unshifted $4snf - 4snh$ intervals. Typical resonances for the two-photon transitions are shown in Fig. 4, and the observed intervals are given in Table II. The typical linewidth of the resonances is 2–3 MHz. The linewidth is due to the Earth's magnetic field since the $4snh$ states are no longer singlets and triplets.

C. Three-photon $4snf \rightarrow 4sni$ intervals

For the three-photon transitions, a single microwave field does not have enough power to drive the three-photon $4snf \rightarrow 4sni$ transitions. Therefore, the three-photon transitions were driven by using two microwave photons and one rf photon. The rf frequency of 3.5–5 GHz frequency was fixed near the $4snh - 4sni$ frequency, and the microwave frequency was swept. We verified that the observed resonances were indeed the $4snf \rightarrow 4sni$ transitions by varying the rf frequency within ±5 MHz and sweeping the microwave frequency for each rf frequency. For each rf frequency, the $4snf \rightarrow 4sni$ interval, given by twice the microwave frequency plus the rf frequency, was approximately constant, with only a slight difference in frequency due to the ac Stark shift. A typical three-photon resonance is shown in Fig. 5. In Fig. 5, we do not see the K splitting, because the K splitting in the $4sni$ states is not resolvable. Since most of the K splitting is from the dipole term, we can estimate the K splitting in the $4sni$ states using the adiabatic dipole term of Eqs. (37) and (38a) and ignoring the quadrupole term of Eq. (38b) of Ref. [10]. Explicitly,

$$K_{n\ell} = \frac{2(2\ell+1)\Delta_{4p}\langle r^{-6}\rangle_{n\ell}\langle 4s|r|4p\rangle^2}{9(W_{4s} - W_{4p})^3}, \tag{2}$$

where Δ_{4p} is the fine-structure splitting of the Ca^+ $4p$ state, $\langle r^{-6}\rangle_{n\ell}$ is the expectation value of $1/r^6$ of the $n\ell$ Rydberg state, $\langle 4s|r|4p\rangle$ is the Ca^+ radial matrix element, W_{4s} is the energy of the Ca^+ $4s$ state, and W_{4p} is the energy of the Ca^+ $4p$ state. Since we have measured the K splitting in the $4snh$ states, we can use Eq. (2) to estimate the K splitting in the $4sni$ states. The ratio between the K splitting in the $4sni$ and $4snh$ states is the ratio $\langle r^{-6}\rangle_{ni}/\langle r^{-6}\rangle_{nh} = 0.2$. Therefore, the K splitting in the $4sni$ states varies from 4 to 2 MHz as n increases from 18 to 23, which is not resolvable in our experiment due to the Earth's magnetic field.

In the three-photon transitions there are both rf and microwave power shifts. To eliminate the ac Stark shift from both fields, we observed the resonances at different rf and microwave powers. For a given microwave power, we observed resonances at different rf powers. We extrapolated the observed frequencies linearly to obtain the resonance frequency at zero

TABLE II. $nf - nh$ observed intervals and nh K splittings.

n	$K = 9/2$ (MHz)	$K = 11/2$ (MHz)	K splitting (MHz)
18	95296.36(6)	95312.53(9)	16.17(11)
19	81300.49(6)	81314.41(3)	13.92(7)
20	69905.16(18)	69917.62(13)	12.46(22)
21	60536.07(10)	60546.51(9)	10.44(13)
22	52761.38(96)	52770.12(12)	8.74(97)
23	46261.65(18)	46269.19(5)	7.54(19)

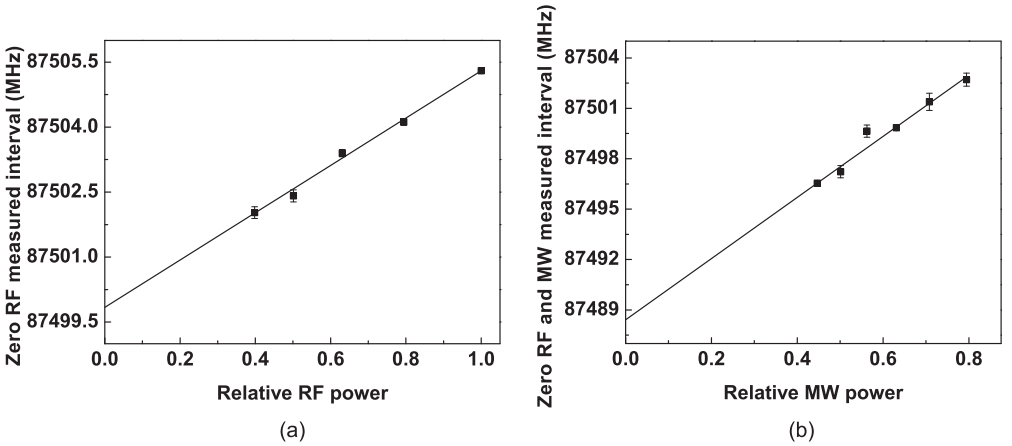

FIG. 6. Extrapolation of the three-photon $4s19f \rightarrow 4s19i$ transition to zero rf and microwave powers. (a) At relative microwave power 0.63, resonances were observed at different rf powers to obtain the resonance frequency at zero rf power. (b) Several zero rf power resonances were obtained at different microwave powers and extrapolated to zero rf and microwave powers.

rf power for a given microwave power. We repeated the same procedure for several microwave powers. The resonance frequencies at zero rf power of several microwave powers were extrapolated to obtain the resonance frequencies at zero rf and microwave powers. A typical resonance is shown in Fig. 6, typical power extrapolations are shown in Fig. 5, and the unshifted intervals are given in Table III.

D. Four-photon $4snf \rightarrow 4snk$ intervals

The $4snf \rightarrow 4snk$ four-photon transitions were excited using two microwave photons and two rf photons. The rf frequency was fixed near the $4snh \rightarrow 4snk$ resonance, while the microwave frequency was swept in the vicinity of the $4snf \rightarrow 4snh$ resonance. Similar to the three-photon excitation, we verified that the observed resonances were the $4snf \rightarrow 4snk$ transitions by varying the rf frequency within ± 5 MHz and sweeping the microwave frequency for each rf frequency. For each rf frequency, the $4snf \rightarrow 4snk$ interval was given by twice the microwave frequency plus twice the rf frequency and was approximately constant. We eliminated the ac Stark shifts using the process discussed for the three-photon transitions. Typical signals for four-photon transitions are shown in Fig. 7, and the unshifted intervals are given in Table IV. Using Eq. (2), we estimate the K splitting in the $4snk$ states to be on the order of 1 MHz for $18 \leqslant n \leqslant 20$, which cannot be resolved in this experiment.

TABLE III. $nf - ni$ observed intervals.

n	Observed frequency (MHz)
18	102558.95(54)
19	87488.41(40)
20	75223.05(15)
21	65141.32(78)
22	56766.61(69)
23	49771.37(26)

E. One-photon $4snf \rightarrow 4s(n+1)d$ intervals

We have observed the $4snf \rightarrow 4s(n+1)d$ transitions for $n = 19$, 20, and 21. In this region the $4snd\ ^1D_2$ Rydberg states are perturbed by their interaction with the $3d^2\ ^1D_2$ state [12]. The perturbation results in shorter lifetimes and rapidly changing quantum defects. For $19 \leqslant n \leqslant 21$ the $4snd\ ^1D_2$ states lie close enough in energy to the $4snf\ ^1F_3$ states that the $4snf \rightarrow 4s(n+1)d$ frequencies are within the microwave frequency range that we can generate. A typical resonance is shown in Fig. 8, and the observed intervals are presented in Table V.

IV. DATA ANALYSIS

We analyze the measured $\Delta\ell$ intervals using several variants of the core polarization model. First, we use the core polarization model as originally introduced by Mayer and Mayer [6]. In the high angular momentum $4sn\ell$ Rydberg states of $\ell > 4$, the Rydberg $n\ell$ electron is assumed to be in a hydrogenic $n\ell$ state which does not penetrate the Ca^+ core.

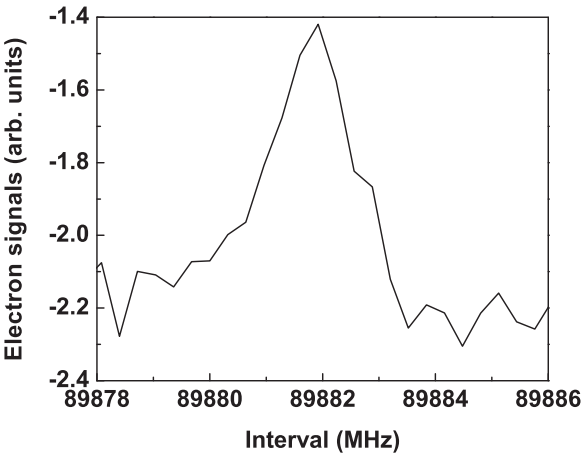

FIG. 7. Four-photon $4s19f \rightarrow 4s19k$ resonance at 0.178 relative microwave power and 0.794 relative rf power. The K splitting of the $4s19k$ states is on the order of 1 MHz and cannot be resolved.

TABLE IV. $nf - nk$ observed intervals.

n	Observed frequency (MHz)
18	105362.90(52)
19	89879.91(7)
20	77278.61(15)

TABLE V. $nf - (n+1)d$ observed intervals.

n	Observed frequency (MHz)
19	84377.04(4)
20	49143.13(12)
21	24542.36(4)

Furthermore, the Rydberg electron is assumed to move slowly compared to the electrons in the ionic core. Thus we term this model the adiabatic core polarization model. The presence of the Rydberg electron leads to a quasistatic electric field and gradient at the Ca^+ core, and, due to the dipole and quadrupole polarizabilities of the core, the energy levels of the Ca $4s n\ell$ states are depressed below the hydrogenic energy, $-1/2n^2$. The polarization energy shift is given by [6]

$$W_{\mathrm{pol},n\ell} = -\tfrac{1}{2}\alpha_d \langle r^{-4}\rangle_{n\ell} - \tfrac{1}{2}\alpha_q \langle r^{-6}\rangle_{n\ell}, \tag{3}$$

where α_d and α_q are the dipole and quadrupole polarizabilities of the Ca^+ $4s$ core, and $\langle r^{-4}\rangle_{n\ell}$ and $\langle r^{-6}\rangle_{n\ell}$ are the expectation values of the squares of the $n\ell$ Rydberg electron's field and field gradient at the core. Since the Rydberg electron is assumed to be in a hydrogenic state, analytic expressions exist for these expectation values. We can write Eq. (3) in Edlen's experimentally convenient form as [13]

$$W_{\mathrm{pol},n\ell} = -\alpha_d P_{n\ell} - \alpha_q P Q_{n\ell}, \tag{4}$$

where

$$P_{n\ell} = R_{\mathrm{Ca}} \langle r^{-4}\rangle_{n\ell} \tag{5}$$

and

$$Q_{n\ell} = \frac{\langle r^{-6}\rangle_{n\ell}}{\langle r^{-4}\rangle_{n\ell}}. \tag{6}$$

Here R_{Ca} is the Rydberg constant for Ca, $R_{\mathrm{Ca}} = 109\,735.81\ \mathrm{cm}^{-1}$. Since we measure the intervals between the $4sn\ell$ and $4sn(\ell+1)$, $\ell > 3$, states of the same n, we express the difference between the core polarization energies of $4sn\ell$ and $4sn(\ell+1)$ states of the same n as follows:

$$\frac{\Delta W_{\mathrm{pol},n\ell'\ell}}{\Delta P_{n\ell\ell'}} = \alpha_d + \alpha_q \frac{\Delta P Q_{n\ell\ell'}}{\Delta P_{n\ell\ell'}}, \tag{7}$$

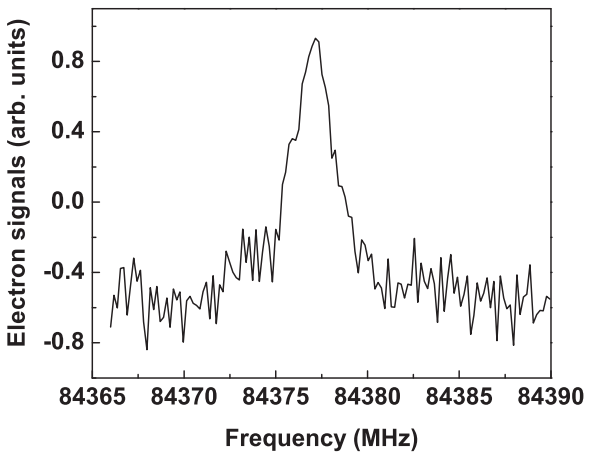

FIG. 8. One-photon $4s19f \rightarrow 4s20d$ resonance.

where $\Delta W_{\mathrm{pol},n\ell'\ell} = W_{\mathrm{pol},n\ell'} - W_{\mathrm{pol},n\ell}$, $\Delta P_{n\ell\ell'} = P_{n\ell} - P_{n\ell'}$, and $\Delta P Q_{n\ell\ell'} = P_{n\ell} Q_{n\ell} - P_{n\ell'} Q_{n\ell'}$. $\Delta P_{n\ell\ell'}$ and $\Delta P Q_{n\ell\ell'}$ are easily calculated, and $\Delta W_{\mathrm{pol},n\ell'\ell}$ is the measured $4sn\ell - 4sn\ell'$ interval. Figure 9 shows the graph of $\frac{\Delta W_{\mathrm{pol},n\ell'\ell}}{\Delta P_{n\ell\ell'}}$ versus $\frac{\Delta P Q_{n\ell\ell'}}{\Delta P_{n\ell\ell'}}$ using the measured $nh - ni$ (▲) and $ni - nk$ (■) intervals. For the $4snh$ states in which the $K = 9/2$ and $11/2$ states are resolved, we use the centers of gravity in our calculation. As suggested by Eq. (7), by plotting $\frac{\Delta W_{\mathrm{pol},n\ell'\ell}}{\Delta P_{n\ell\ell'}}$ versus $\frac{\Delta P Q_{n\ell\ell'}}{\Delta P_{n\ell\ell'}}$, the values of dipole and quadrupole polarizabilities can be extracted from the y intercept and slope of a line through the data points, as shown in Fig. 9. The resulting Ca^+ $4s$ dipole and quadrupole polarizabilities are $\alpha_d = 75.32(4)a_0^3$ and $\alpha_q = -257(8)a_0^5$, respectively. In this, its simplest form, the adiabatic core polarization model yields a negative quadrupole polarizability, which is impossible.

van Vleck and Whitelaw pointed out that the polarization energy shift of Eq. (3) is a limiting case of a second-order shift due to the higher multipole terms in the Coulomb interaction between the Rydberg $n\ell$ electron and the ion core [14]. For example, the dipole polarization energy of a Ca $4sn\ell$ state comes from the dipole coupling to $Npn'(\ell \pm 1)$ and $Np\epsilon(\ell \pm 1)$ bound and continuum states, as shown in Fig. 10. By considering only the two valence electrons we are implicitly ignoring inner-shell excited states of Ca, which amounts to ignoring the contribution of the Ca^{++} polarizability to the Ca^+ polarizability. The shift due to the higher lying $Npn'(\ell \pm 1)$ and $Np\epsilon(\ell \pm 1)$ states is readily calculated in second-order perturbation theory by summing over N and n', and integrating

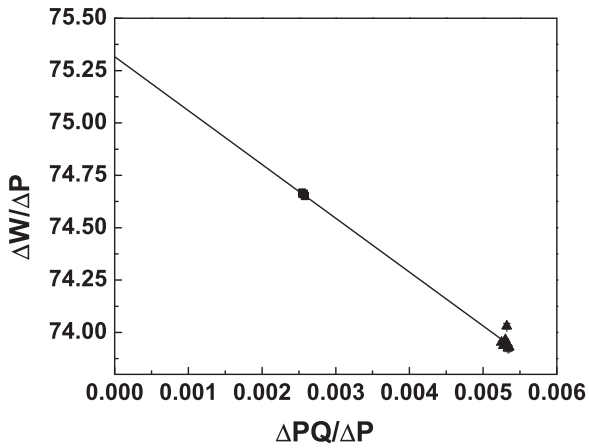

FIG. 9. Adiabatic plot of the measured $nh - ni$ (▲) and $ni - nk$ (■) intervals using Eq. (7). There are three data points for the $ni - nk$ (■) intervals, $18 \leqslant n \leqslant 20$, and six data points for the $nh - ni$ (▲) intervals, $18 \leqslant n \leqslant 23$. A fit to the straight line yields the y intercept and slope, which are α_d and α_q, respectively. The resulting fit values are $\alpha_d = 75.32(4)a_0^3$ and $\alpha_q = -257(8)a_0^5$.

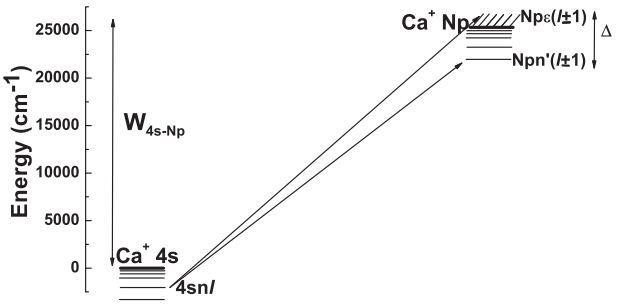

FIG. 10. Energy levels of the Rydberg states converging to the Ca^+ $4s$ and Np states and the continua associated with the latter. A $4sn\ell$ Rydberg state is dipole coupled to $Npn'(\ell \pm 1)$ states which span an energy range Δ. If $\Delta \ll W_{4s-Np}$ the adiabatic approximation is valid.

over ϵ. The sum over n' and the integral over ϵ span an energy range Δ, as shown by Fig. 10. If

$$\Delta \ll W_{4s-Np}, \tag{8}$$

for all N, the result of Mayer and Mayer is recovered. For example, the dipole polarization energy shift is given by the dipole term of Eq. (3). Equation (8) is a more precise statement of the adiabatic condition. For alkali-metal atoms, in which the excited states of the ion are all at high energies, the requirement of Eq. (8) is easily met, and the adiabatic approximation works well. For alkaline-earth atoms this requirement is not met, and the adiabatic approximation fails, as is evident in Fig. 9.

To correct for the nonadiabatic effects and extract the core polarizabilities from the $\Delta\ell$ intervals there are two approaches we can take. One is the adiabatic expansion method, which can be viewed as an expansion in powers of Δ/W_{4s-Np}. The attraction of this approach is that we are only calculating the corrections to the analytic shifts obtained using hydrogenic expectation values. The potential problem is convergence of the expansion. The alternative approach is the direct numerical calculation of the hydrogenic matrix elements for the dipole and quadrupole interactions, as exemplified in Fig. 10. This approach is in principle exact, but since the entire energy shift is calculated numerically, small errors are important.

In the adiabatic expansion approach the higher-order terms in the expansion appear as expectation values of higher inverse powers of r. If the expansion is to converge, these terms should become smaller with increasing order. While this condition is met for the high ℓ states, it is not for the $4snh$ states. In the nonadiabatic correction to the dipole polarization energy the $\langle r^{-8}\rangle_{n\ell}$ term is larger than the $\langle r^{-6}\rangle_{n\ell}$ term. In short, the expansion is nonconvergent, and we cannot use this method to analyze our data. However, using the leading correction term for the dipole polarization energy provides a bound for the polarizabilities. The leading term in the correction to the dipole polarization energy has a $\langle r^{-6}\rangle_{n\ell}$ dependence and is thus indistinguishable from the quadrupole polarization energy. With the inclusion of this term, Eq. (7) becomes

$$\frac{\Delta W_{\mathrm{pol},n\ell\ell'}}{\Delta P_{n\ell\ell'}} = \alpha_d + (\alpha_q - 6\beta_1)\frac{\Delta PQ_{n\ell\ell'}}{\Delta P_{n\ell\ell'}}, \tag{9}$$

where $\beta_1 \cong 0.95\alpha_d/(2W_{4p-4s})$ [15]. The numerical factor of 0.95 comes from the fact that 5% of α_d comes from higher-lying np states of Ca^+ and Ca^{++} [16]. We calculate $6\beta_1$ to be $1850(40)a_0^5$. Including the leading term in the adiabatic expansion simply raises the value of α_q by $6\beta_1$, yielding $\alpha_q = 1590(40)a_0^5$. The value of α_d is unchanged. Since the $6\beta_1$ correction term in Eq. (9) overcorrects for the nonadiabatic effect, these values are lower and upper bounds to α_d and α_q, respectively.

TABLE VI. k_d calculated values.

n	$\ell = 5$	$\ell = 6$	$\ell = 7$
18	0.956528	0.972293	0.982680
19	0.956518	0.972178	0.982543
20	0.956500	0.972111	0.982437
21	0.956437	0.972033	
22	0.956453	0.971906	
23	0.956423	0.971892	

The alternative approach is the direct calculation of the multipole interactions, as shown in Fig. 10 for the dipole interaction. As an approximation we assume that all the dipole and quadrupole polarization energies of the Ca $4sn\ell$ states come from the couplings to the Ca $4pn'\ell'$ and $3dn'\ell'$ states. For both the dipole and quadrupole shifts, we find the ratio of the explicitly calculated shift to that predicted by the adiabatic model. These ratios, the nonadiabatic factors k_d and k_q, are then used to correct the adiabatic model. Explicitly, we rewrite Eq. (3) as

$$W_{\mathrm{pol},n\ell} = -\tfrac{1}{2}k_d\alpha_d\langle r^{-4}\rangle_{n\ell} - \tfrac{1}{2}k_q\alpha_q\langle r^{-6}\rangle_{n\ell}. \tag{10}$$

The nonadiabatic factors k_d and k_q are defined in Eqs. (17.25) and (17.26) of Ref. [17]. Both are calculated numerically using a Numerov algorithm to calculate hydrogenic wave functions. The calculated values of k_d and k_q are given in Tables VI and VII, respectively. There are sum rules for the sums of the squares of the matrix elements [14], and using them we estimate the percentage uncertainties in k_d and k_q to be 0.3% for both values. As shown in Table VI, to three significant digits, there is no n dependence in k_d. As shown in Table VII, to four significant digits, there is n dependence in k_q for $\ell = 5$ and $\ell = 6$ but not for $\ell = 7$. We can express Eq. (10) in Edlen's form as follows:

$$W_{\mathrm{pol},n\ell} = -\alpha_d P'_{n\ell} - \alpha_q P' Q'_{n\ell}, \tag{11}$$

where

$$P'_{n\ell} = k_d P \tag{12}$$

TABLE VII. k_q calculated values.

n	$\ell = 5$	$\ell = 6$	$\ell = 7$
18	0.9780	0.9273	0.9376
19	0.9797	0.9277	0.9376
20	0.9812	0.9284	0.9376
21	0.9824	0.9284	
22	0.9835	0.9287	
23	0.9845	0.9292	

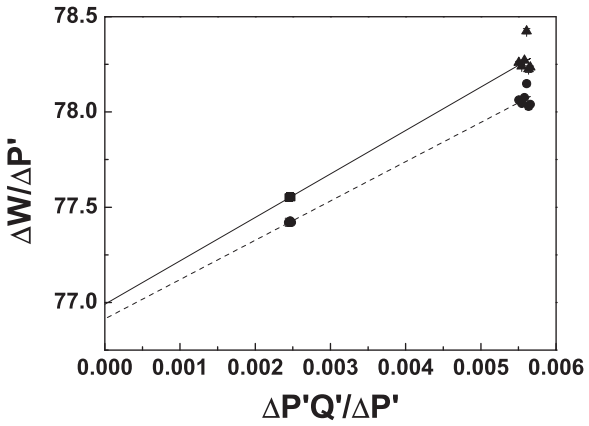

FIG. 11. Nonadiabatic plot of the measured $nh - ni$ (▲) and $ni - nk$ (■) intervals using Eq. (14). There are three data points for the $ni - nk$ (■) intervals, $18 \leqslant n \leqslant 20$, and six data points for the $nh - ni$ (▲) intervals, $18 \leqslant n \leqslant 23$. A linear fit (solid line) gives values for the y intercept and slope of $76.99(7)a_0^3$ and $228(12)a_0^5$, respectively. When we take into account the overcorrection of k_d, we obtain the data points (•) and the lower fit line (broken line), which leads to our final values of $\alpha_d = 76.91(5)a_0^3$ and $\alpha_q = 206(9)a_0^5$.

and

$$Q'_{n\ell} = \frac{k_q}{k_d} Q_{n\ell}. \tag{13}$$

Hence the difference between the core polarization energy of $4sn\ell$ and $4sn\ell'$ of the same n is

$$\frac{\Delta W_{\mathrm{pol},n\ell'\ell}}{\Delta P'_{n\ell\ell'}} = \alpha_d + \alpha_q \frac{\Delta P' Q'_{n\ell\ell'}}{\Delta P'_{n\ell\ell'}}, \tag{14}$$

where $\Delta W_{\mathrm{pol},n\ell'\ell}$ is defined in Eq. (7), $\Delta P'_{n\ell\ell'} = P'_{n\ell} - P'_{n\ell'}$, and $\Delta P' Q'_{n\ell\ell'} = P'_{n\ell} Q'_{n\ell} - P'_{n\ell'} Q'_{n\ell'}$.

We plot $\frac{\Delta W_{\mathrm{pol},n\ell'\ell}}{\Delta P'_{n\ell\ell'}}$ versus $\frac{\Delta P' Q'_{n\ell\ell'}}{\Delta P'_{n\ell\ell'}}$ in Fig. 11 using the $nh - ni$ (▲) and $ni - nk$ (■) measured intervals. From Fig. 11, the intercept and slope of the graph yield fit values of $\alpha_d = 76.99(7)a_0^3$ and $\alpha_q = 228(12)a_0^5$, respectively, shown by the solid line.

At this point it is useful to compare Figs. 9 and 11, in particular the points on the solid line in Fig. 11. There is almost no difference in the horizontal positions of the data points but a large difference in their vertical positions, leading to very different values for α_q. The difference in the vertical positions comes from substituting $\Delta P'$ for ΔP, i.e., introducing k_d, the nonadiabatic correction to the dipole polarization energy. The small difference in the horizontal positions of the points in the two graphs indicates that the introduction of k_q, the nonadiabatic correction for the quadrupole polarization energy, has a negligible effect for these $\Delta\ell$ intervals. The uncertainties in the fit in Fig. 11 do not reflect the uncertainty in the calculation of k_d. When it is taken into account the values we obtain are $\alpha_d = 77.0(3)a_0^3$ and $\alpha_q = 228(12)a_0^5$.

We now return to our assumption that the polarization shifts are due entirely to the couplings to the $4pn'\ell'$ and $3dn'\ell'$ states. This assumption is equivalent to assuming the Ca^+ polarizabilities arise entirely from the Ca^+ $4p$ and $3d$ states. The calculations of Safronova and Safronova indicate that 95% of α_d is due to the $4p$ state, and 58% of α_q is due to the $3d$ state [16]. Thus in k_d and k_q we have overcorrected. Inspecting Figs. 9 and 11 we can see that the overcorrection due to k_q is insignificant, but that due to k_d is important. Accordingly, we have reduced the correction due to k_d by 5%, resulting in the broken line in Fig. 11. This modification leads to the values $\alpha_d = 76.91(5)a_0^3$ and $\alpha_q = 206(9)a_0^5$. When the uncertainty in the calculation of k_d is taken into account the values we obtain are $\alpha_d = 76.9(3)a_0^3$ and $\alpha_q = 206(9)a_0^5$. As we shall discuss shortly, we believe these values to be upper and lower bounds to α_d and α_q.

TABLE VIII. Ca^+ $4s$ dipole polarizability (α_d) obtained from this work and other theoretical and experimental results.

	α_d (a_0^3)
This work$_{ae}$	75.32(4)
This work$_{dc}$	76.9(3)
Expt. [8]	87(2)
Expt. [18]	75.3(4)
Expt. [19]	70.89(15)
Theory [16]	76.1(5)
Theory [21]	73.0(1.5)
Theory [20]	75.49

V. DISCUSSION

Tables VIII and IX show values of α_d and α_q from this work and other experimental and theoretical work. The uncertainties for our values represent the uncertainties from the fits of the data to the two models. The values labeled $_{ae}$ are from the adiabatic expansion method, Eq. (9), and the values labeled $_{dc}$ are from the direct calculation method, Eq. (14). There are three experimental results for α_d to which we can compare ours. The value of Ref. [8] is based on the measurement of the $4snf \rightarrow 4sng$ intervals. The analysis of these data relied heavily on a more complex theoretical model, which was probably inadequate to represent the $4sng$ states. The value of α_d given in Ref. [18] was obtained by assuming that the $4snh$ quantum defects arise solely from the dipole polarizability and applying the adiabatic core polarization model. Since the quadrupole polarizability is small and the nonadiabatic effect on the dipole polarization cancels its effect to some extent, this approach yields a value for α_d close to the value we obtained from Fig. 9. In Ref. [19] lifetime measurements of the Ca^+ $4p_j$ states were used to obtain the oscillator strengths of the $4s - 4p_j$ transitions, taking into account the small branching ratios for decay to the $3d_j$ states. The oscillator strengths of the $4s - 4p_j$ transitions were then used to calculate the value

TABLE IX. Ca^+ $4s$ quadrupole polarizability (α_q) obtained from this work and other theoretical results.

	α_q (a_0^5)
This work$_{ae}$	1590(40)
This work$_{dc}$	206(9)
Theory [16]	871(4)
Theory [20]	875.1

of α_d. The resulting value of α_d is too small due to the neglect of higher-lying Ca^+ Np states and the dipole polarizability of Ca^{++}, but when this omission is taken into account it is consistent with our value for α_d. The theoretical values for α_d from Refs. [16] and [20] fall within our experimental bounds given in Eq. (15), while the theoretical value of Ref. [21] is clearly outside the bounds.

As shown in Table IX, our value for α_q obtained by the adiabatic expansion method is twice the theoretical value, and the value obtained by the direct calculation method is a factor of 4 smaller than the theoretical value. Since a large fraction, two-thirds, of the quadrupole polarizability is due to the Ca^+ $3d$ states, an alternative check of the calculated quadrupole polarizability is the lifetime of the Ca^+ $3d$ state, which decays by quadrupole radiation. The measured lifetime is in good agreement with the calculated lifetime, supporting the validity of the calculation of α_q. It is worth noting that if the value of k_d for the $4snh$ states is reduced to 98.35% of the current k_d value we would obtain $\alpha_d = 75.3(1)a_0^3$ and $\alpha_q = 878(15)a_0^5$, in excellent agreement with the recent theoretical values. In view of the sensitivity of the direct calculation approach to the numerical calculations of k_d and the large discrepancy between our value of α_q and the theoretical values, we view the direct calculation values of Tables VIII and IX as upper and lower bounds for α_d and α_q, respectively. As a consequence, we report bounds for α_d and α_q. Explicitly,

$$75.3a_0^3 < \alpha_d < 76.9a_0^3 \tag{15}$$

and

$$206a_0^5 < \alpha_q < 1590a_0^5. \tag{16}$$

Our ability to specify α_d and α_q is limited by our confidence in the core polarization models. Two experimental avenues can be explored to minimize this problem. The first is measuring higher ℓ intervals in which the nonadiabatic corrections are not as large, as done by Lundeen *et al.* for other atoms [22]. The second is high-resolution laser spectroscopy of the Ca $4snd$ $^1D_2$ states. Absolute measurements of their energies, good to 10 MHz, would locate the $4snd$ levels relative to the hydrogenic $n\ell$ levels. The microwave measurements reported here could then be used to locate the Ca $4sn\ell$ levels relative to the H $n\ell$ levels, and the present data could then be analyzed in terms of the displacements of the energies from the hydrogenic levels, instead of the differences in the displacements. The $4snh$ states could be dropped from the analysis, substantially reducing the uncertainty due to the nonadiabatic corrections.

Making measurements involving higher ℓ states should minimize the nonadiabatic effects, allowing a better determination of the polarizabilities. However, it is not obvious that the discrepancy between the theoretical and experimental values will disappear. Intervals between the high ℓ Ba $6sn\ell$ levels have been measured, but the value of α_q extracted by the direct calculation method is a factor of 2 smaller than the theoretical value, a similar discrepancy to that reported here for Ca [23]. Determining the source of these discrepancies is a worthy theoretical challenge.

VI. CONCLUSION

We have measured $\Delta\ell$ intervals of Ca $4snf \rightarrow 4sn\ell$, $18 \leqslant n \leqslant 23$, and $4 \leqslant \ell \leqslant 7$ using a microwave and rf resonance approach. We have used these measurements to place bounds on the Ca^+ dipole and quadrupole polarizabilities. The Ca^+ $4s$ dipole and quadrupole polarizabilities are $75.3a_0^3 < \alpha_d < 76.9a_0^3$ and $206a_0^5 < \alpha_q < 1590a_0^5$. The Ca^+ $4s$ dipole polarizability agrees well with recent theoretical values. However, we are not able to place tight bounds on the Ca^+ $4s$ quadrupole polarizability due to uncertainties in the core polarization analyses. We hope this work will motivate theoretical work to reexamine the problem of core polarization analysis and, more generally, the source of the discrepancy between the experimental and theoretical values of α_q.

ACKNOWLEDGMENTS

This work has been supported by the U.S. Department of Energy, Office of Basic Energy Sciences. J.N. would like to thank DPST Research Grant No. 030/2557, Thailand Research Fund (TRF) Grant No. MRG5680117, and CMU Junior Research Fellowship Program for their supports. It is a pleasure to acknowledge F. S. Niyaz for assistance in the measurements, M. Safronova for pointing out the paucity of measurements for Ca, and S. R. Lundeen for many insightful discussions.

[1] R. J. Hendricks, J. L. Sorensen, C. Champenois, M. Knoop, and M. Drewsen, Phys. Rev. A **77**, 021401(R) (2008).
[2] M. Kajita, Y. Li, K. Matsubara, K. Hayasaka, and M. Hosokawa, Phys. Rev. A **72**, 043404 (2005).
[3] M. Chwalla, J. Benhelm, K. Kim, G. Kirchmair, T. Monz, M. Riebe, P. Schindler, A. S. Villar, W. Hänsel, C. F. Roos, R. Blatt, M. Abgrall, G. Santarelli, G. D. Rovera, and Ph. Laurent, Phys. Rev. Lett. **102**, 023002 (2009).
[4] B. Arora, M. S. Safronova, and C. W. Clark, Phys. Rev. A **76**, 064501 (2007).
[5] T. F. Gallagher and W. E. Cooke, Phys. Rev. Lett. **42**, 835 (1979).
[6] J. E. Mayer and M. G. Mayer, Phys. Rev. **43**, 605 (1933).
[7] U. I. Safronova and M. S. Safronova, Phys. Rev. A **79**, 022512 (2009).
[8] A. G. Vaidyanathan, W. P. Spencer, J. R. Rubbmark, H. Kuiper, C. Fabre, D. Kleppner, and T. W. Ducas, Phys. Rev. A **26**, 3346 (1982).
[9] E. S. Shuman, J. Nunkaew, and T. F. Gallagher, Phys. Rev. A **75**, 044501 (2007).
[10] E. S. Shuman and T. F. Gallagher, Phys. Rev. A **74**, 022502 (2006).
[11] E. L. Snow, R. A. Komara, M. A. Gearba, and S. R. Lundeen, Phys. Rev. A **68**, 022510 (2003).
[12] T. R. Gentile, B. J. Hughey, D. Kleppner, and T. W. Ducas, Phys. Rev. A **42**, 440 (1990).

[13] B. Edlen, *Handbuch der Physik* (Springer, Berlin, 1964).
[14] J. H. Van Vleck and N. G. Whitelaw, Phys. Rev. **44**, 551 (1933).
[15] E. L. Snow and S. R. Lundeen, Phys. Rev. A **76**, 052505 (2007).
[16] M. S. Safronova and U. I. Safronova, Phys. Rev. A **83**, 012503 (2011).
[17] T. F. Gallagher, *Rydberg Atoms* (Cambridge University Press, Cambridge, England, 1994).
[18] E. S. Chang, J. Phys. B **16**, L539 (1983).
[19] C. E. Theodosiou, L. J. Curtis, and C. A. Nicolaides, Phys. Rev. A **52**, 3677 (1995).
[20] J. Mitroy and J. Y. Zhang, Eur. Phys. J. D **46**, 415 (2008).
[21] B. K. Sahoo, B. P. Das, and D. Mukherjee, Phys. Rev. A **79**, 052511 (2009).
[22] S. R. Lundeen, in *Advances in Atomic, Molecular, and Optical Physics*, edited by P. R. Berman and C. C. Lin (Academic Press, New York, 2005), Vol. 52.
[23] E. G. Kim, J. Nunkaew, and T. F. Gallagher, Phys. Rev. A **89**, 062503 (2014).